

See discussions, stats, and author profiles for this publication at: <https://www.researchgate.net/publication/351791857>

Multi-scale, multi-sensor data integration for automated 3-D geological mapping

Article in *Ore Geology Reviews* · May 2021

DOI: 10.1016/j.oregeorev.2021.104252

CITATIONS

54

READS

859

8 authors, including:



[Sam Thiele](#)

Helmholtz-Zentrum Dresden-Rossendorf

52 PUBLICATIONS 1,386 CITATIONS

[SEE PROFILE](#)



[Sandra Lorenz](#)

Helmholtz-Zentrum Dresden-Rossendorf

75 PUBLICATIONS 935 CITATIONS

[SEE PROFILE](#)



[Cecilia Contreras](#)

Helmholtz-Zentrum Dresden-Rossendorf

23 PUBLICATIONS 358 CITATIONS

[SEE PROFILE](#)

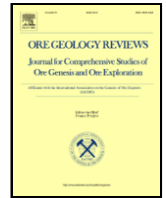


[Laura Tusa](#)

Helmholtz-Zentrum Dresden-Rossendorf

31 PUBLICATIONS 565 CITATIONS

[SEE PROFILE](#)



Multi-scale, multi-sensor data integration for automated 3-D geological mapping

Samuel T. Thiele^a, Sandra Lorenz^a, Moritz Kirsch^a, I. Cecilia Contreras Acosta^{a, b}, Laura Tusa^{a, b}, Erik Herrmann^a, Robert Möckel^a, Richard Gloaguen^a

^a Helmholtz-Zentrum Dresden-Rossendorf, Helmholtz Institute Freiberg for Resource Technology, Chemnitz Str. 40, 09599 Freiberg, Germany

^b TheiaX, HZDR Innovation, Bautzner Landstraße 400, 01328 Dresden, Germany

ARTICLE INFO

Keywords:

Hypercloud
Hyperspectral
Digital outcrop geology
Machine learning
Corta Atalaya
hylite

ABSTRACT

Enhanced digital outcrop models attributed with hyperspectral reflectance data, or hyperclouds, provide a flexible, three-dimensional medium for data-driven mapping of geological exposures, mine faces or cliffs. This approach allows the collection of spatially contiguous information on exposed mineralogy and so provides key information for understanding mineralising processes, interpreting 1-D drillhole data, and optimising mineral extraction. In this contribution we present an open-source python workflow, *hylite*, for creating hyperclouds by seamlessly fusing geometric information with data from a variety of hyperspectral imaging sensors and applying necessary atmospheric and illumination corrections. These rich datasets can be analysed using a variety of techniques, including minimum wavelength mapping and spectral indices to accurately map geological objects from a distance. Reference spectra from spectral libraries, ground or laboratory measurements can also be included to derive supervised classifications using machine learning techniques. We demonstrate the potential of the hypercloud approach by integrating hyperspectral data from laboratory, tripod and unmanned aerial vehicle acquisitions to automatically map relevant lithologies and alterations associated with volcanic hosted massive sulphide (VHMS) mineralisation in the Corta Atalaya open-pit, Spain. These analyses allow quantitative and objective mineral mapping at the outcrop and open-pit scale, facilitating quantitative research and smart-mining approaches. Our results highlight the seamless sensor integration made possible with *hylite* and the power of data-driven mapping approaches applied to hyperclouds. Significantly, we also show that random forests (RF) trained only on laboratory data from labelled hand-samples can be used to map outcrop scale data.

1. Introduction

Open-pit and underground face mapping is an essential part of any mining operation, as it facilitates optimal ore extraction and guides future exploration. However, access limitations make face mapping a challenging and potentially dangerous task, and geologists on the ground must make the most of limited time and safety restrictions during mapping. For this reason, a variety of methods have been developed for the remote mapping of open-pits or underground mine faces (e.g., Boubanga-Tombet et al., 2018; Fraser et al., 2006; Kirsch et al., 2018; Krupnik and Khan, 2019; Kurz et al., 2011; Lorenz et al., 2018; Murphy et al., 2015; Murphy and Monteiro, 2013; Yang et al., 2013; Ramanaidou and Wells, 2012; Kruse et al., 2012).

Previous remote mapping methods have focused on two types of data: two-dimensional (2-D) hyperspectral imagery, from which com-

positional information can be inferred, and detailed geometric reconstructions ('digital outcrops') containing important three-dimensional (3-D) information. High and ultra-high resolution point clouds, such as those generated using light detection and ranging (LiDAR) and ground or unmanned aerial vehicle (UAV) photogrammetry have become widely used datasets in the earth sciences (Bemis et al., 2014; Dering et al., 2019; Nesbit et al., 2018). In addition to detailed geometry, these datasets typically contain colour or reflectivity information that are useful for discriminating geological lithologies and structures. However, many rock-types have indistinguishable signatures in the visible part of the spectrum, so visible near infrared (VNIR; 400 to 1000 nm) or short-wave infrared (SWIR; 1000 to 2500 nm) hyperspectral data are needed. A significant body of literature exists on geological mapping with hyperspectral data (see van der Meer et al., 2012, for a review) but, as this field has emerged from the satellite remote-sensing commu-

s.thiele@hzdr.de

<https://doi.org/10.1016/j.oregeorev.2021.104252>

Received 23 November 2020; Received in revised form 14 April 2021; Accepted 19 May 2021
0169-1368/© 2021

nity, high fidelity 3-D information is typically unavailable and rarely included (Fraser et al., 2006; Kurz et al., 2011; Buckley et al., 2013; Lorenz et al., 2018; Salehi et al., 2018; Kirsch et al., 2018, 2019).

Recent studies have bridged the gap between the digital outcrop and hyperspectral approaches by fusing high-resolution point clouds with high spectral resolution imagery to create ‘hyperclouds’ (Buckley et al., 2013; Kirsch et al., 2019, 2018; Kurz et al., 2011; Lorenz et al., 2018; Salehi et al., 2018). These datasets have significant potential in the earth sciences, as they allow the integrated representation of both geometric and spectral characteristics. Hyperclouds improve our ability to infer the usually complex composition, mineralogy and structure of natural geological formations and thus to generate precise and quantitative maps for research or industry.

In this contribution, we restructure and extend the Mephysto hyperspectral toolbox (Jakob et al., 2017) to present an open-source library for (1) correcting hyperspectral images, (2) locating imaging positions and camera-poses relative to high resolution point clouds, (3) seamlessly back-projecting one or more hyperspectral datasets into three-dimensions, and (4) analysing the results. Our aim is to provide a powerful and flexible software platform with which the research community can easily generate atmospheric and geometrically corrected hyperclouds for successful data integration, synthesis, analysis and interpretation. We also strive to make this functionality accessible to non-specialists by including interactive and easy-to-use Jupyter notebooks (Kluyver et al., 2016) for useful processing workflows.

To illustrate the potential of this approach for geological mapping, we apply it to ground and UAV hyperspectral data from the Rio Tinto mine, which is considered to host the largest massive sulphide deposit of the Iberian Pyrite Belt, Spain. The following sections describe a complete processing workflow for integrating laboratory, tripod, and UAV-borne hyperspectral images, generating geometrically corrected 3-D hyperclouds, and the application of machine learning methods to analyse the results and produce a geological map of a structurally complex open-pit mine.

2. Geological setting

The Rio Tinto area is located ~ 70 km north of Huelva in the Iberian Pyrite Belt (IPB), a 300 km long and 80 km wide fold and thrust belt extending from southern Portugal into southern Spain (Fig. 1a). The IPB contains more than 100 volcanic-hosted massive sulfide (VHMS) deposits, making it one of the most significant concentrations of mineral deposits in Europe (Inverno et al., 2015; Leistel et al., 1997). The area has a rich mining history dating back to the Bronze Age, while currently active mining operations and recent exploration successes demonstrate that significant resources remain.

Corta Atalaya (henceforth abbreviated as CA) is one of the largest open-pit mines in Europe, with a size of 1200 × 900 m and depth of ca. 350 m. It was constructed in 1907 to exploit the San Dionisio ore body, which was mined until 1992. Currently, mining activity is focussed on the adjacent Cerro Colorado open-pit mine, but exploration activities surrounding CA are ongoing. The San Dionisio ore body is located on the southern flank of a Variscan-aged, km-scale, southward-vergent antiformal stack system that exposes strata of the Late Devonian to Lower Carboniferous Volcanic Sedimentary Complex (Diez-Montes et al., 2017). At CA, this unit is composed of basaltic to intermediate volcanic rocks outcropping along the northern part of the pit, and overlying felsic volcanic rocks, slate and conglomerate which are exposed in the western part of the mine (Diez-Montes et al., 2017). The sequence is capped by a transition series including hydrothermally altered purple shale, an important marker horizon in the IPB that has an affinity with massive sulphide mineralisation (Soriano and Marti, 1999), and syn-orogenic flysch sediments (greywackes and slates) of the Mississippian to Pennsylvanian Culm Group. Both of these units are exposed in the southern part of the pit.

Sulfide mineralisation occurs as pyritic and cupriferous stockwork (considered to be feeder zones to the massive sulfides) within the basic to felsic volcanics, and as dismembered lenses of stratabound massive sulphides within the uppermost felsic volcanics at CA (Martin-Izard et al., 2015). All rocks of the Rio Tinto area are intensely altered due to low grade regional metamorphism and hydrothermal activity associated with mineralization. The shale, mafic volcanics and stockwork generally exhibit a chloritic alteration that increases in intensity towards the mineralization (Diez-Montes et al., 2017), whereas the felsic volcanic rocks show a zoned alteration, with pervasive sericitization cross-cut by a later chlorite-rich alteration proximal to mineralization (Martin-Izard et al., 2015). In near-surface areas and adjacent to faults a locally significant silica to chlorite-rich alteration is also present.

The entire complex is cross-cut by a series of E-W striking Variscan thrusts, and locally offset by a conjugate set of late strike-slip faults with NW-SE trending dextral and NE-SW trending sinistral kinematics. Additionally, an extensional detachment has been mapped at the interface between the volcanic rocks and the Culm, often in spatial proximity of massive sulfide ore bodies (Quesada, 1997).

3. Photogrammetric survey

A photogrammetric survey of the CA open-pit was conducted to generate a high-resolution digital outcrop model. A Nikon D850 DSLR camera and Nikkor 85 mm f/1.8G lens was used to acquire 488 RGB photographs from multiple viewpoints around and within the pit. Agisoft Metashape Professional v1.6 was then used to generate a photogrammetric reconstruction (see Appendix 1 for details), and the resulting point cloud georeferenced by means of co-registration to 1 m resolution airborne LiDAR data (PNOA-LiDAR from the Spanish government) using the iterative closest point method implemented in CloudCompare (Girardeau-Montaut, 2020).

4. Hyperspectral data processing with *hylite*

Hyperspectral imagery was captured using a tripod mounted AisaFENIX hyperspectral sensor (Spectral Imaging Ltd., Oulu, Finland) and UAV-borne Rikola sensor (Rikola Ltd., Oulu, Finland). Additionally, the spectral characteristics of hand samples collected during field campaigns were measured under laboratory conditions using the AisaFENIX mounted on a drill core scanner. In the following section we outline the pre-processing workflows implemented in *hylite* (Fig. 2), and their application to the CA dataset. Complete descriptions of each method and their implementation can be found in the appendices accompanying this publication, and the *hylite* documentation (<https://tinyurl.com/hylite-docs>). The *hylite* source code and detailed Jupyter notebooks covering each processing workflow can also be downloaded from GitHub (<https://tinyurl.com/hylite>).

4.1. Laboratory acquisition

Imaging hyperspectral scanners for hand specimens and drill cores are increasingly being used to analyse lithology and mineralogy at the mm–cm scale (Acosta et al., 2019; Tuşa et al., 2020). Hyperspectral acquisition under laboratory conditions (e.g. controlled lighting, small source-target-sensor distances) allows for detailed and accurate spectral characterisation of hand samples and drill cores with relatively limited processing (Fig. 2a).

Fifty-seven hand samples representing the lithologies exposed at CA were scanned using a SiSuROCK drill-core scanner equipped with an AisaFENIX hyperspectral sensor (Spectral Imaging Ltd., Oulu, Finland). *hylite* was then used to convert each raw Fenix dataset to radiance by subtracting a dark-reference and applying sensor calibrations, and to reflectance using a white calibration panel (Appendix 2). Geometric

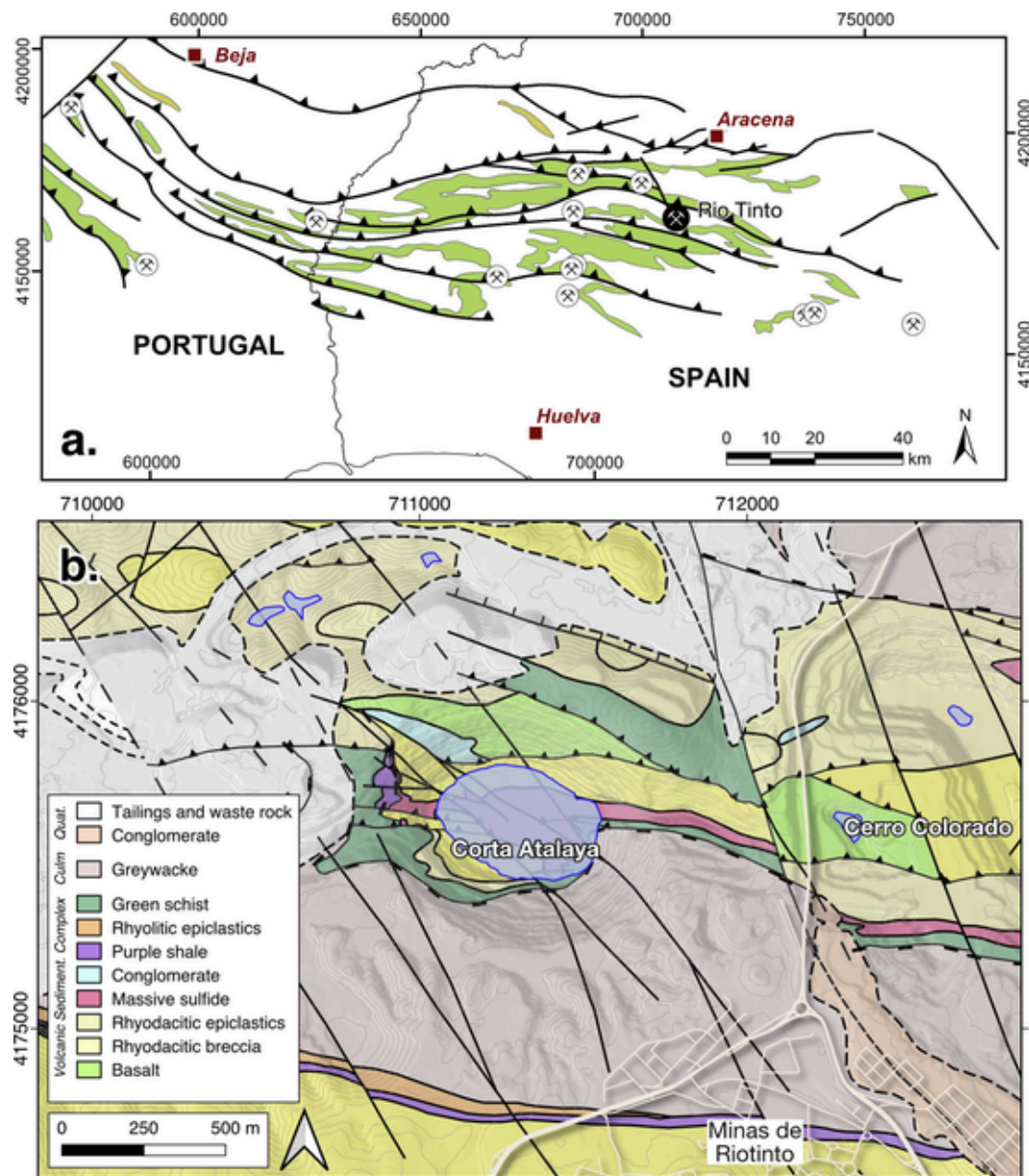


Fig. 1. Overview map of the Iberian Pyrite belt (a) with locations of the main massive sulfide deposits hosted in the Late Devonian to Early Carboniferous Volcanic Sedimentary Complex (green). Map modified from Martin-Izard et al. (2015). The geology of the Corta Atalaya and Cerro Colorado open pits, as mapped by Díez-Montes and García-Crespo (2013), is also shown (b).

lens-distortion was also corrected for, resulting in a set of planimetric images with a pixel size of ~ 1.5 mm.

The scanned hand-samples were segmented using a semi-automatic grab-cut algorithm (Appendix 3; Rother et al., 2004). Spectra from each of these were then used to create a spectral library, define spectral lithotypes, and to create a labelled training dataset for subsequent supervised classification (Section 5). To mitigate challenges comparing laboratory spectra with outcrop spectra acquired under less controlled conditions, a robust and handcrafted feature set based on spectral indices and minimum wavelength maps (Section 5.2) was used for this supervised classification (Section 5.3).

4.2. Tripod acquisition

The AsiaFENIX can be mounted on a tripod and used to acquire panoramic outcrop scans using a rotary stage (cf., Kirsch et al., 2019; Lorenz et al., 2018). Unlike the laboratory SiSuROCK configuration,

the resulting image must be corrected for atmospheric and illumination effects before meaningful reflectance estimates can be derived (Fig. 2b). Geometrically complex scenes (such as the open-pit at CA) also require data capture from multiple overlapping viewpoints to ensure complete coverage.

As previously described for the laboratory acquisition, the raw Fenix imagery was converted to radiance by applying a dark reference and spectral calibration followed by geometric lens corrections (cf., Appendix 2). R90 Spectralon calibration panels were placed in each scene and oriented sub-parallel to the mine face. These were then automatically identified in the imagery (Appendix 4) and used to extract a white-reference spectrum that characterises the spectral composition of the downwelling light illuminating each scene. Note that these panels could not be placed on the outcrop itself, so do not account for the influence of the (relatively short) optical path length between the outcrop and sensor. Furthermore, unlike the core-scanning configuration, the illumination is unevenly distributed so an additional correction, re-

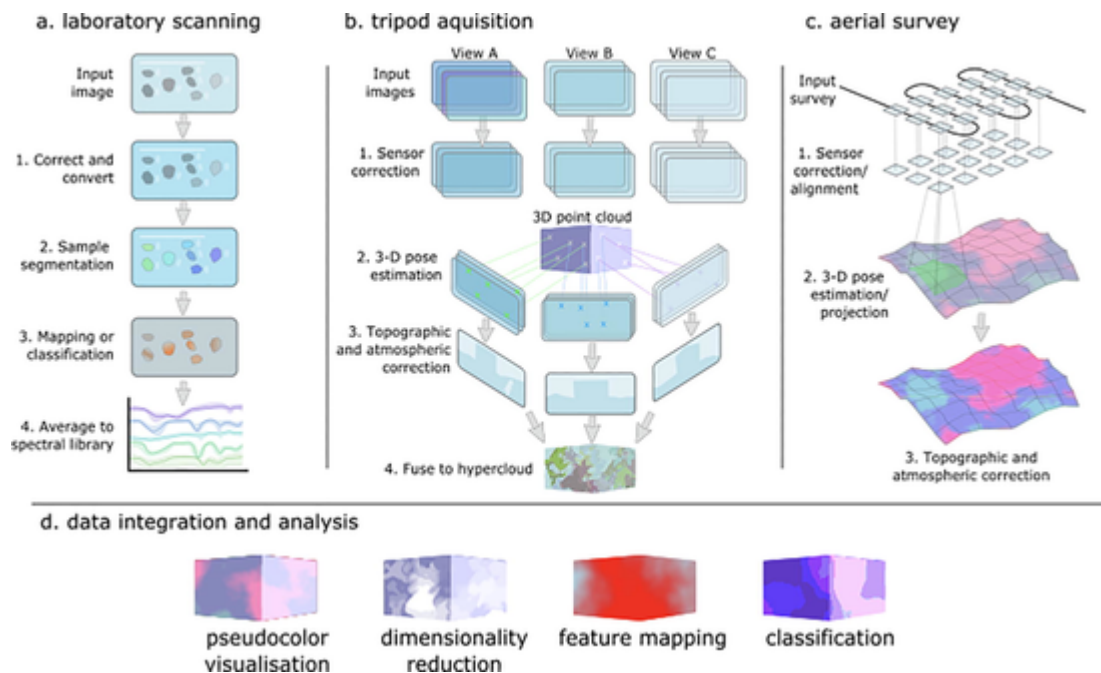


Fig. 2. Overview of the *hylite* workflow for correcting and localising laboratory (a), tripod (b) and airborne, e.g. UAV-based, hyperspectral data (c). These different data can be integrated to create and analyse hyperspectral point clouds (d).

quiring information on the scene geometry, is needed before pixel reflectance can be estimated. It is also worth noting that atmospheric gases with strong absorption features, such as water vapour, largely obscure parts of the spectra, and make direct comparisons with laboratory spectra challenging. Wavelengths associated with the deepest water features (900–1000, 1100–1200, 1300–1550 and 1750–2050 nm) were thus excluded from further processing.

Digital outcrop models acquired using photogrammetry or LiDAR, such as the photogrammetric model of CA described in Section 3, contain geometric information that is the same or higher resolution than the corresponding hyperspectral scene. It is theoretically possible to perform an accurate illumination correction, although a recent review of illumination correction methods (Jakob et al., 2017) suggest that methods developed for satellite remote sensing often perform poorly at the outcrop scale. A selection of correction methods are implemented in *hylite*, including the cosine, c-factor and minnaert algorithms (cf., Jakob et al., 2017).

The first step of any illumination correction is the co-registration of hyperspectral imagery and geometric surface orientation data. In *hylite* this is achieved by implementing panoramic and perspective camera models (for pushbroom- and frame-sensors respectively) that allow seamless projection of data between a 3-D reference point cloud (digital outcrop model) and each hyperspectral dataset. These camera models require accurate knowledge of camera position and orientation (pose), which typically cannot be measured in the field using standard equipment.

Limited knowledge of camera pose is circumvented in *hylite* by matching features between the 3-D point cloud and hyperspectral images and then solving the well known Perspective-n-Point (PnP) problem using Open-CV (Appendix 5; Bradski and Kaehler, 2008). First, an approximate camera pose estimate based on field measurements is used to render the 3-D point cloud and extract scale invariant features (SIFT; Lowe, 1999) that are matched with similar features identified in the red, green and blue channels of the hyperspectral scene using the fast library for approximate nearest neighbours algorithm (FLANN; Muja and Lowe, 2009). As the real-world position of pixels in the point cloud render is known, it is thus possible to calculate the 3-D position of matching features in the hyperspectral dataset. These features with

known image and real-world coordinates are then used to optimise the camera pose using the PnP solution and RANSAC outlier detection implemented in OpenCV (Bradski and Kaehler, 2008). Note that 2-D image coordinates in panoramic cameras (such as the Fenix) are first transformed to an equivalent perspective projection before solving the PnP problem. Refined camera pose information is then stored in the image header metadata for easy subsequent access.

Geometric information such as surface orientation can now be projected into each hyperspectral scene using the refined camera pose information. At this point, all the necessary information for atmospheric and illumination corrections are available, using one of the various methods implemented in *hylite*. Accurate illumination corrections are essential to derive meaningful outcrop reflectance spectra, though remain a significant challenge for near-surface remote sensing approaches deploying UAVs and tripod-mounted sensors (Jakob et al., 2017; Lorenz et al., 2018).

For the Corta Atalaya dataset, a novel joint illumination correction was applied. Illumination across the scene was modelled as a mixture of downwelling sunlight and skylight. By comparing the difference in radiance measured between shadowed and non-shadowed regions, and assuming these regions had the same median reflectance, it was possible to estimate the ambient skylight spectrum and so decompose the spectra measured for the R90 Spectralon calibration panels into a sunlight and ambient skylight spectra. Scene geometry and sunlight incidence angle was then used to estimate the intensity of these two light sources at every pixel, and thus reconstruct per pixel illumination across the scene. As sensor to target distances were generally small (< 1 km), path radiance effects were considered negligible (outside of the atmospheric water absorption bands mentioned previously), so illumination corrected pixel reflectance estimates were derived by dividing each pixel by its reconstructed illumination spectra. A full description of this novel correction method is beyond the scope of this study, but is the subject of an upcoming publication. Other state of the art atmospheric and topographic correction methods implemented in *hylite* are described in detail by Jakob et al., (2017) and Lorenz et al., (2018).

Finally, reflectance estimates from each hyperspectral scene can be back-projected onto the point cloud and averaged (or blended based on some other metric such as ground sampling distance or orientation), re-

sulting in a homogeneous 3-D hyperspectral point cloud. For the CA dataset, a total of 10 ground based scenes from 5 different viewing locations were back-projected and corrected using this workflow, resulting in a hypercloud of the open-pit with 3,242,964 points and 257 bands.

4.3. UAV acquisition

UAV-hyperspectral imaging is a rapidly developing field, as previously large and heavy sensor technology is now miniaturised. Hyperspectral frame-sensors covering the visible and near-infrared range are available (see Aasen et al., 2018 for a review), while several companies have also recently developed UAV capable pushbroom sensors that cover the short-wave infrared (Aasen et al., 2018; Zhong et al., 2018). Pushbroom sensors typically come with manufacturer software for geometric correction, however most frame-based sensors lack such established workflows. The high-frequency movements typical of UAV-platforms present significant challenges for the accurate georeferencing and band-alignment of frame-based sensors and, while some authors have developed specific corrections (Honkavaara et al., 2016, 2012; Jakob et al., 2017), no widely usable solution is available yet. Additional corrections such as reflectance conversion, masking and topographic/illumination corrections are comparable challenges to those described in the previous section about tripod acquisition.

hylite contains a complete workflow for the alignment, back-projection, correction and fusion of frame-based hyperspectral UAV data (Fig. 2c). We have also implemented this in a way that allows correction workflows for new sensors to be easily added.

The *hylite* correction workflow for UAV imagery can be found in Appendix 6. As an initial step, internal radiometric and geometric corrections such as dark current subtraction, the application of gain and offset values and the geometric correction of internal optical distortions are applied. Individual hyperspectral bands are then aligned to a predefined reference band by calculating an affine transform using SIFT features (Lowe, 1999) and FLANN point matching (Muja and Lowe, 2009). This rough alignment is adjusted to account for topographic distortions by calculating the optical flow between adjacent bands (using the Open-CV implementation of deepflow; Weinzaepfel et al., 2013) and removing the identified pixel offsets. Individual camera positions and orientations are then identified using either the PnP solution described in Section 4.2 or, for large UAV surveys, using external photogrammetric software.

For the CA case study, Agisoft Metashape Professional v1.6 was used to align 357 Rikola datacubes captured during two subsequent UAV surveys of the western portion of the open pit. Pseudo-true-color image derivatives (R: 687.554, G: 559.527, B: 511.96 nm) were used to perform this alignment. *hylite* was used to perform a lens correction on the data prior to photogrammetric reconstruction, and the lens distortion coefficients in Metashape kept fixed at zero during the bundle adjustment. These camera pose estimates were then used by *hylite* to back-project all of the hyperspectral bands onto the high resolution point cloud. The resulting hypercloud was corrected for atmospheric and illumination effects using the same workflow described in Section 4.2, and subsequently fused with the Fenix data as described in Section 4.4. Hypercloud products were also converted to georeferenced orthomosaics for use with external GIS software.

4.4. Data fusion

A big advantage of the hypercloud approach is that an arbitrary number of datasets can be back-projected onto a single point cloud and compared or fused based on the spectral or geometric attributes of each point. For the CA case study, the Rikola hyperspectral data intensities were adjusted using more accurate but lower spatial resolution Fenix data using histogram equalisation (Appendix 7). These high spatial res-

olution spectra were then fused with VNIR bands of the Fenix hypercloud to increase resolution in the area covered by Rikola imagery. To minimise distortions due to the nadir orientation of the Rikola camera and oblique viewing angles of the Fenix imagery, the two datasets were merged using point averages with a weighting factor equal to the z-component of each point's normal vector. Thus, spectra on horizontal planes are dominantly derived from the high resolution Rikola imagery, and spectra on vertical planes from the Fenix imagery.

5. Results: Data analysis and integration

A key design feature of *hylite* is its use of polymorphic structures to represent various hyperspectral data (e.g., spectral libraries, images, hyperclouds) in a uniform way. Hence, standard analysis techniques such as minimum wavelength mapping or hull correction can be just as easily applied to a spectral library as a hypercloud. This is fundamental to facilitating data integration between, for example, spectra acquired using a field spectrometer, a ground-based hypercloud and aerial imagery.

In the following section we demonstrate this approach, and the variety of analysis tools implemented in *hylite*, by integrating Sisurock imagery of hand-samples with a hypercloud derived from terrestrial and UAV imagery to map the geology of the CA open-pit.

5.1. Qualitative analysis and visualisation

As a preliminary data exploration step, *hylite* was used to create a series of true (Fig. 3a) and false-colour visualisations of the scanned hand samples and CA hypercloud. False-colour representations were created using wavelengths in the SWIR (2200.0, 2250.0 and 2350.0 nm) that are sensitive to clay, chlorite and mica mineralogy (Fig. 3b; Vedder and McDonald, 1963; Loh, 1973; Pontual et al., 1997; Laukamp et al., 2021), and using the widely applied minimum noise fraction (MNF; Green et al., 1988) dimensionality reduction technique (Fig. 3c), following the implementation in SPY (Boggs, 2014). Interactive 3-D visualisations of the hypercloud and its various derivatives can be viewed at <https://tinyurl.com/ca-hypercloud>.

With these visualisations as a reference, each hand-sample was classified into nine spectral lithologies (Fig. 4) based on interpretations of individual pixel spectra (Table 1). These lithologies were carefully chosen such that they are (1) spectrally distinguishable and (2) geologically meaningful. Hence, they are largely defined by the abundance of spectrally active phases such as clay, mica, chlorite and iron oxide. General reflectance characteristics such as brightness and flatness were also considered when distinguishing lithologies without diagnostic absorption features (e.g. shale and massive sulphide). X-ray diffraction mineralogy was also performed on selected samples to validate our spectral interpretations (Appendix 8) and clarify the mineral associations that cause the observed spectral features.

5.2. Quantitative measurement and feature extraction

Direct comparison of spectra acquired by different sensors and/or in disparate environments (e.g. laboratory vs. outdoors) remains a significant challenge. However some spectral derivatives, such as spectral indices (e.g., band ratios) and minimum wavelength maps, are remarkably robust to variations in scale, acquisition method and illumination. We take advantage of these products (e.g., Cudahy et al., 2008; Sonntag et al., 2012; Haest et al., 2012; van Ruitenbeek et al., 2014; Hecker et al., 2019; van der Meer et al., 2018) and construct a feature set that can be used to directly compare spectral characteristics between hand-sample and open-pit scales, with the principal aim of training a supervised classifier on labelled hand-samples and applying it to map lithology in the CA hypercloud.

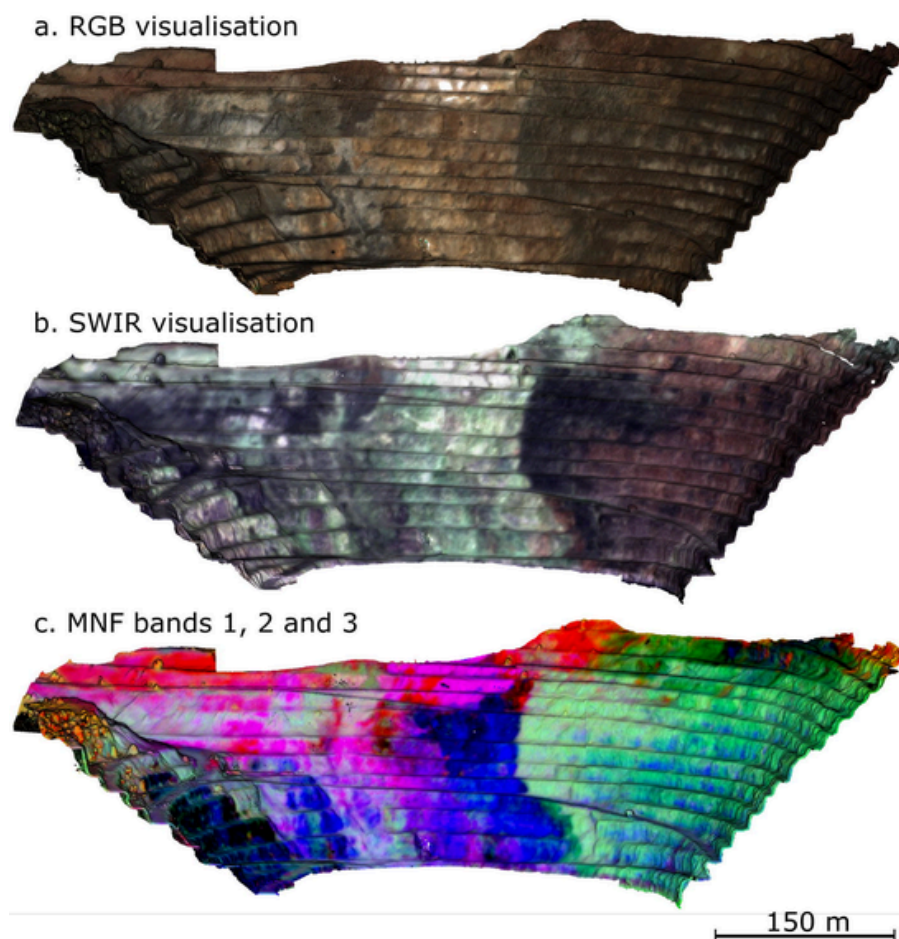


Fig. 3. Colour composites of the CA hypercloud created using *hylite* and showing a true-colour ($R = 680.0$ nm, $G = 550.0$ nm, $B = 500.0$ nm) visualisation (a), false-colour visualisation ($R = 2200.0$ nm, $G = 2250.0$ nm, $B = 2350.0$ nm) highlighting variations in clay, chlorite and mica content (b), and the first three MNF bands (c). 3-D visualisations of these data can be found at <https://tinyurl.com/ca-hypercloud>.

A wide variety of spectral indices have been developed for extracting geological information from multi- and hyperspectral data. As these are typically applied on remotely sensed satellite data they avoid spectral bands sensitive to atmospheric effects, and so can be applied on both outdoor and laboratory data. Arbitrarily complex spectral indices can be calculated using *hylite* using inbuilt tools for spectral resampling and combination, or through direct manipulation of the underlying data array using *numpy* (Harris et al., 2020). We extract 12 geologically sensitive spectral indices (Table 2) from the core-scanner imagery and hypercloud data. These indices were developed by Cudahy et al., (2008) to map the geology of the Mt Isa region using ASTER and airborne hyperspectral data, and are sensitive to mica, clay, carbonate and iron oxide minerals. The results (Fig. 5; Appendix 9) are directly comparable between the laboratory and outdoor datasets, and highlight similarities and differences between the various spectral-lithologies defined in Section 5.1.

Minimum-wavelength (MWL) maps are also commonly applied to map the distribution of specific minerals using hyperspectral data (Hecker et al., 2019). For example, the position of specific absorption features in the short-wave infrared region are very sensitive to the length of AlOH, FeOH and MgOH bonds in silicate minerals, allowing accurate discrimination between a variety of clay, mica, chlorite, carbonate and amphibole minerals (Hecker et al., 2019; van der Meer et al., 2018; van Ruitenbeek et al., 2014). Minimum wavelength maps were calculated for the CA datasets (Fig. 6, Appendix 9) by fitting three gaussian functions to a hull corrected spectra from 2120 to 2350 nm.

As shown by Figs. 5 and 6, and Appendix 9, the spectral indices and MWL maps for the laboratory and outdoor datasets are quantitatively comparable. Hence, we propose that they represent a set of geologically relevant features that are, at least in this case study, invariant to scale and acquisition method.

5.3. Automated geological mapping

The indices and minimum wavelength maps described in Section 5.2. provide a method for directly comparing spectra acquired under field and laboratory conditions. This opens the possibility of training a supervised classifier using the library of classified hand samples (Fig. 4) and then applying it to automatically map the geology of the CA open pit. In the following section we explore this option, developing a hand-tailored decision tree that can distinguish between the main alteration minerals at CA, and training a random forest algorithm that can perform lithological mapping.

5.3.1. Alteration mapping using a decision tree

Similar to previous studies investigating mineral alteration (e.g., Cudahy et al., 2008; Clark et al., 2003) we mapped the distribution of sericite and chlorite (Fig. 7), which are often associated with hydrothermal alteration in VHMS deposits, using a decision tree based on distinctive spectral characteristics of each mineral. The presence/absence of diagnostic spectral absorptions at 2160, 2200 and 2255 nm (cf. Pontual et al., 1997) was mapped using a depth cutoff of 10%, and the decision tree used to separate kaolinitic clay (feature at 2160 nm),

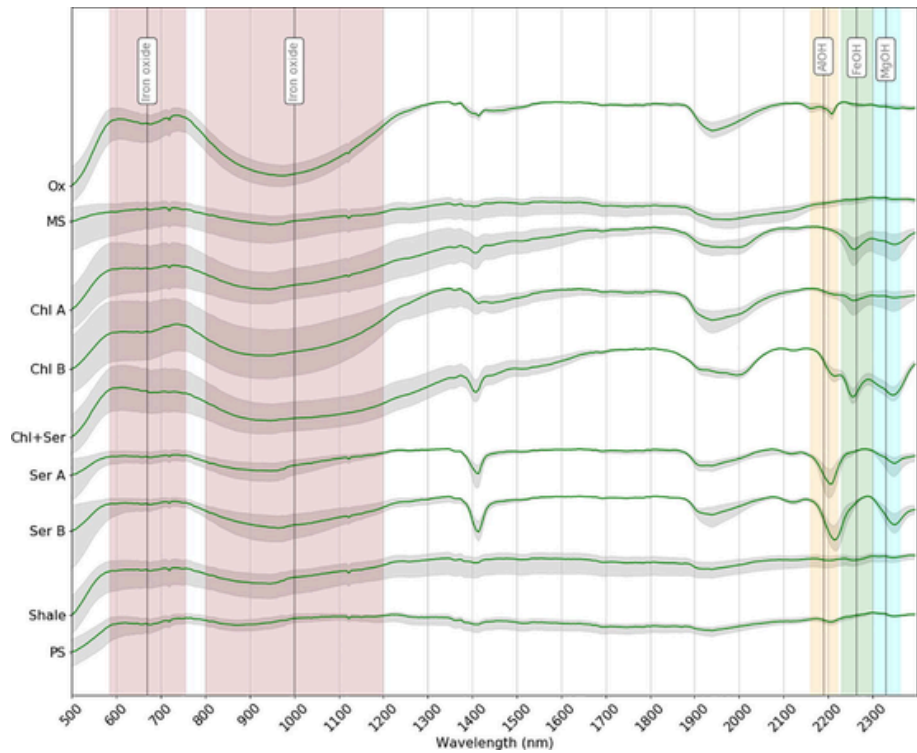


Fig. 4. Spectral library presenting hull corrected median-spectra (green) and associated interquartile area (grey) calculated on all pixels of the hand samples (cf. Figs. 5, 6) representing each of the spectral lithologies interpreted at CA: Oxidised (Ox), massive sulphide (MS), two varieties of chlorite (Chl A and B), two sericitic units (Ser A and B), shale and purple shale (PS). The approximate position of characteristic absorption features (Pontual et al., 1997) are also plotted for reference. See Table 1 for detailed spectral descriptions.

Table 1
Spectral descriptions of the characteristic features (cf. Pontual et al., 1997; Laukamp et al., 2021) of each spectral lithology used during supervised classification (Section 5.3). Spectra for each of these lithologies are plotted in Fig. 4.

| AlOH feature | FeOH feature | MgOH feature | Defining characteristics | Spectral lithology |
|----------------|--------------|--------------|--|--|
| 2160 + 2200 nm | | | Deep iron absorption features and small double-AlOH feature due to associated kaolinite. Flat spectra with broad water feature at 2000 nm. | Oxidised (Ox) Massive sulphide (MS) |
| | ~2260nm | ~2340nm | Double absorption at 2260 and 2340 nm typical of chlorite, limited AlOH absorption at 2200 nm and low intensity broad water feature between 1900 and 2000 nm | Chlorite A (Chl A) |
| | ~2260nm | ~2340nm | As with Chl A but with deeper water features around 1900 nm likely due to the presence of minor sericite. Lower intensity of FeOH and MgOH features | Chlorite B (Chl B) |
| ~2200 nm | ~2260nm | ~2340nm | Distinct AlOH feature from sericite at ± 2200 nm and FeOH feature from chlorite at ± 2260 nm. | Sericite and Chlorite (Ser + Chl) |
| 2204 nm | | ~2340nm | Distinct AlOH feature with minima at 2204 nm (muscovitic composition). High crystallinity indicated by difference in depth of AlOH and water feature (crystallinity = 0.87). | Sericite A (Ser A) |
| 2214 nm | | ~2340nm | Muscovite transitioning towards phengite (AlOH feature located at ± 2214). Depth of water feature relative to AlOH feature suggests increased water content (crystallinity = 0.81). Flat spectra, but distinct from MS due to smaller narrower water feature between 1900 and 2000 nm, low AlOH and FeOH absorption feature and steeper slope between 500 and 600 nm. | Sericite B (Ser B) |
| | | | As above, but with lower slope between 500 and 600 nm and slightly deeper AlOH feature. | Shale Purple shale (PS) |

white mica (feature at 2200 nm but not 2255 nm), chlorite (feature at 2255 nm but not 2200 nm) and chlorite/white mica mixtures (feature at 2200 and 2255 nm). Additionally, mica and chlorite composition was split based on the position of the 2200 nm and 2255 nm absorptions respectively, allowing discrimination of compositional endmembers. Implementation details of this decision tree are included in Appendix 10.

5.3.2. Lithology mapping using random forests

The geology of the CA pit was also investigated using a random forest classifier implemented using Scikit-learn (Pedregosa et al., 2011). Hyperspectral images of labelled hand samples (Section 4.1) were used

as training data, and the resulting model applied to map lithologies in the hypercloud of the CA pit (cf. Appendix 11). As described in Section 5.2, the use of robust and geological meaningful features such as spectral indices and minimum wavelength maps is key to this approach, as it allowed quantitative comparison between hand-sample scale spectra acquired in a laboratory and outcrop scale spectra acquired outdoors.

The random forest method is an ensemble learning classifier; a large set of decision tree classifiers are trained such that their individual results combine to give a consensus classification. Each tree contributes a unit vote, and the final classification label is allocated based on the class with the most votes. These ensembles of tree classifiers are expected to perform more robustly and accurately than an individual decision tree classifier (Breiman, 2001).

Table 2

Spectral indices used to characterise and compare sample and outcrop mineralogy. The colon indicates that an average reflectance was calculated for all bands within the specified range. All wavelengths are in nanometers.

| Index | Definition |
|--------------------------|---|
| AlOH Group content | $(2145:2185 + 2235:2285) / 2185:2225$ |
| AlOH Group composition | $2145:2185 / 2235:2285$ |
| MgOH Group content | $(2185:2225 + 2360:2430) / (2235:2285 + 2295:2365)$ |
| MgOH Group composition | $2235:2285 / 2295:2365$ |
| FeOH Group content | $(2185:2225 + 2295:2365) / 2235:2285$ |
| Ferrous Iron Index | $2145:2185 / 1600:1700$ |
| Ferric Oxide content | $1600:1700 / 780:860$ |
| Ferric Oxide composition | $630:690 / 520:600$ |
| Kaolin Group index | $2185:2225 / 2145:2185$ |
| Opaque index | $520:600 / 1600:1700$ |
| Regolith Index 1 | $780:860 / 2235:2285$ |
| Regolith Index 2 | $1600:1700 / 2235:2285$ |

As with many machine learning methods, results obtained using random forests can be sensitive to hyperparameters that control, for example, tree structure and depth. As is standard practice (Breiman, 2001), we performed a five-fold cross validation to optimise these hyperparameters. A total of 500 combinations of hyperparameters were tested using a forest of 1000 trees. The range of hyperparameter values that were tested, and their optimum value, is summarised in Table 3. During the training phase the classifier achieved accuracies of $\pm 95\%$ on both training and testing subsets of the hand-sample image. Note that these accuracies are not representative of the algorithm's application to the hypercloud data, as for this dataset the ground truth is not known.

The results of the random forest classification are summarised as 3-D visualisations of the classified hypercloud in Fig. 8. The distribution of lithologies show excellent spatial consistency (even though no spatial filtering has been applied), and outline geologically reasonable geometries that generally match with previous mapping (Fig. 1). Bedding measurements extracted using the Compass plugin in CloudCompare (Thiele et al., 2017) along contacts of the clearly folded shale unit

outcropping in the north-east of the pit (the “Corta Atalaya conglomerate”) define a fold axis plunging 8° towards 097° and axial surface dipping at 65° towards 011° . These measurements are broadly consistent with the general structure of the regional geology (Díez-Montes and García-Crespo, 2013), and allowed us to develop an updated interpretation of the structure of CA (Fig. 9).

6. Discussion

Complex geometries and illumination effects make remote sensing of cliffs and open-pit mines with hyperspectral imaging a significant challenge (Jakob et al., 2017; Lorenz et al., 2018). The workflow presented in this contribution, and implemented in the open-source *hylite* python package, helps ameliorate these issues by providing methods for back-projecting, correcting and fusing hyperspectral and geometric data from a variety of sensors. The resulting reflectance spectra are stored in a flexible hypercloud format, such that data from hundreds of individual hyperspectral images can be integrated into a single product for visualisation, interpretation and analysis. The 3-D nature of this approach mitigates occlusion and distortion issues that limit approaches relying on orthographic projection, and facilitates crucial corrections of illumination and atmospheric effects in the hyperspectral data.

The CA case study illustrates the potential of this approach applied to quantitative geological mapping of an open-pit mine. Chloritic and sericitic alteration associated with mineralisation could be mapped using a simple decision tree (Fig. 7), while stratigraphically important horizons such as the purple shale were successfully mapped using random forests (Fig. 8). Significantly, both 3-D maps distinguish subtle variations in mineral chemistry, including the transition towards muscovitic sericite close to the massive sulphide mineralization and lithological variations in chlorite composition. These provide useful analogues for mineralization vectors during future exploration projects, and hint at the potential for multi-scale hyperspectral investigations that integrate data from regional, mine and drill core scales.

The complex but geologically reasonable geometries delineated by the random forests mapping result from the series of tectonic deformations that the host rocks have been subjected to, and provide important insight into the structure of the deposit. For example, our results clearly show that the cryptic “Corta Atalaya conglomerate” unit has been folded into an antiformal structure (Fig. 9). This was missed during pre-

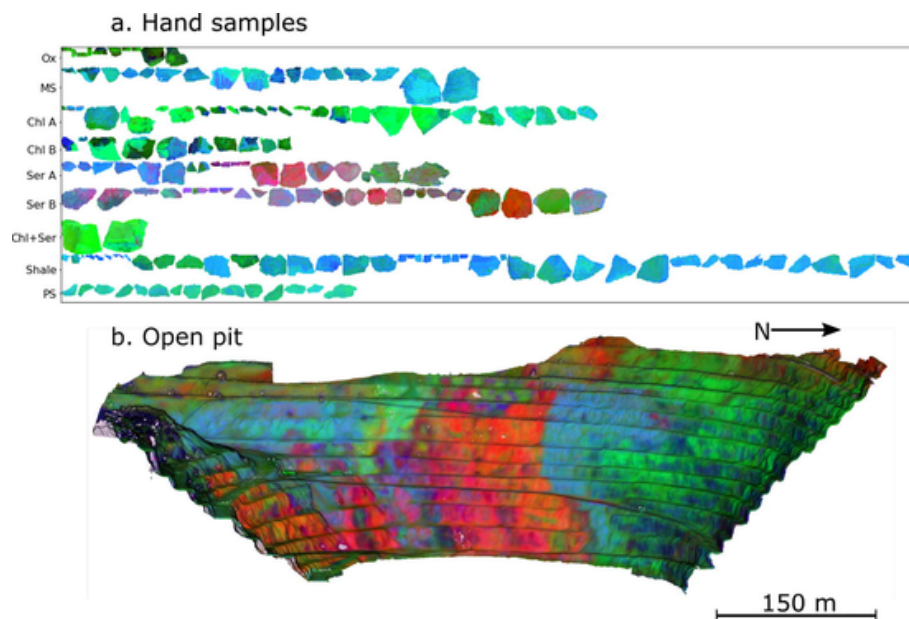


Fig. 5. False colour composite visualisation generated by mapping the AlOH, Ferrous and Opaque indices defined in Table 2 to red, blue and green respectively for the laboratory hand sample scans (a) and hypercloud (b). 3-D visualisations of these data can be found at <https://tinyurl.com/ca-hypercloud>.

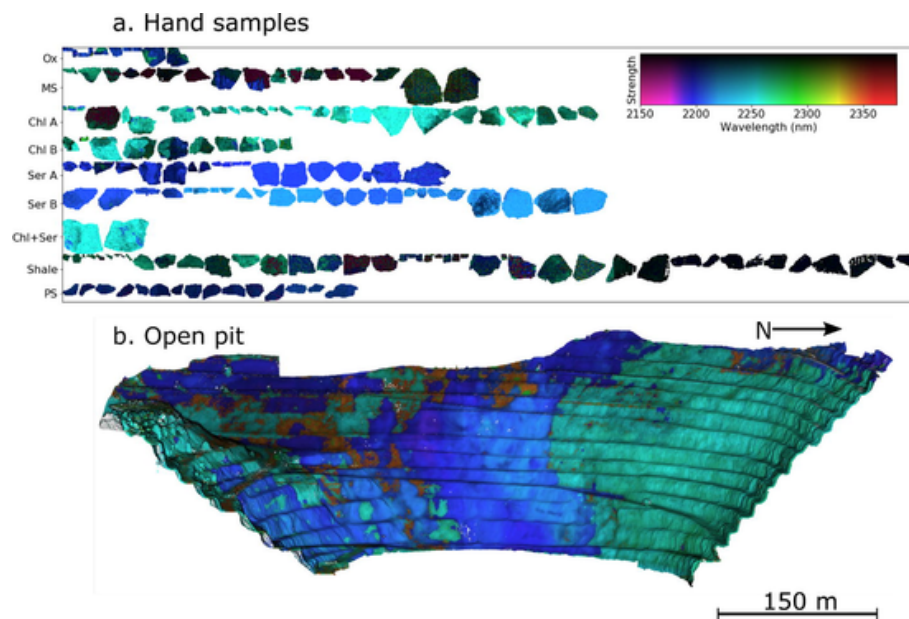


Fig. 6. Minimum wavelength map of the deepest absorption feature between 2120 and 2350 nm, calculated by fitting three gaussian features to this range and selecting the deepest one. Results for hand samples (a) and open pit hypercloud (b) show excellent agreement. Colour represents feature position and brightness the feature depth. Chloritic rocks with a deep FeOH feature are highlighted in green, while mica or clay rich lithologies with a deep AlOH feature appear in purple and blue. Abbreviations correspond to those defined in Fig. 4 and Table 1. 3-D visualisations of these data can be found at <https://tinyurl.com/ca-hypercloud>.

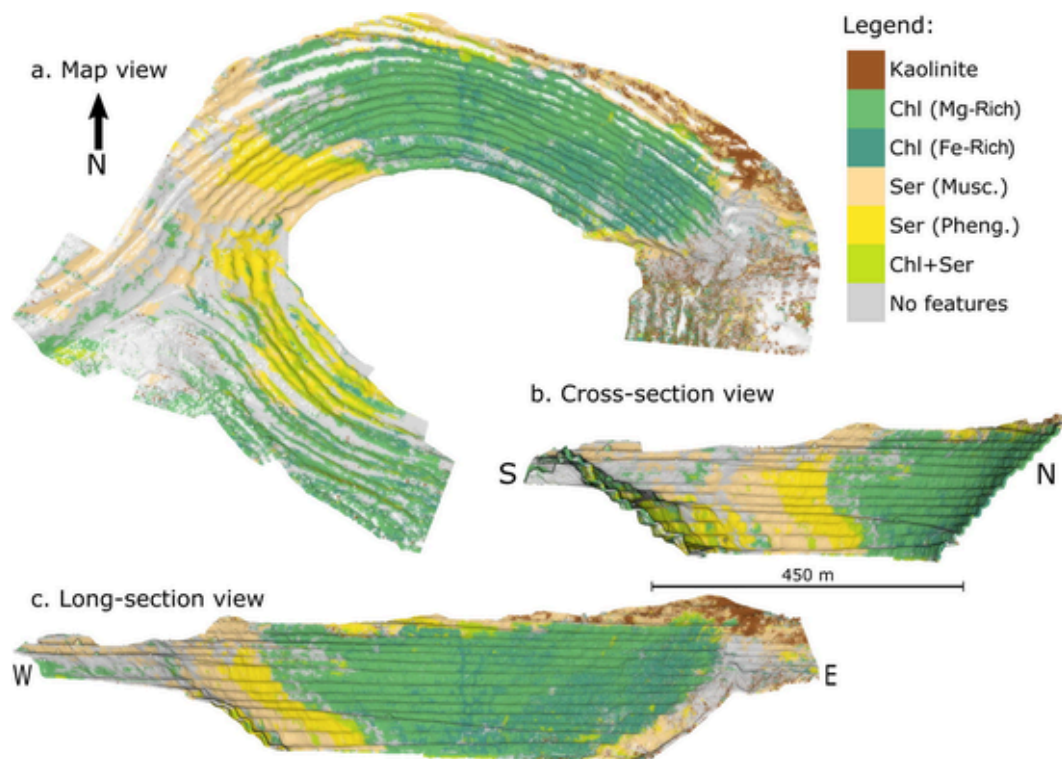


Fig. 7. Distribution of alteration minerals with distinctive alteration features in the SWIR generated by passing the multi-feature minimum wavelength maps (Fig. 6) through a decision tree. The results highlight the muscovitic sericite alteration proximal to the massive sulphide mineralisation, Mg-rich regional chloritic alteration and more Fe-rich chlorites associated with alteration along faults and within the stockwork zone of the deposit. A mica and clay rich zone near the surface is also evident, which we interpret to result from recent weathering. This map can be viewed in 3-D at <https://tinyurl.com/ca-hypercloud>.

vious mapping campaigns (e.g., Díez-Montes and García-Crespo, 2013), presumably due to the difficulties distinguishing this lithology and accessing the relevant outcrops. The hypercloud mapping results and associated structural measurements (Figs. 7 and 8) have thus al-

Table 3

Hyperparameter values tested during hyperparameter optimisation, and their corresponding values. For a detailed description of each hyperparameter please refer to the scikit learn documentation.

| Hyperparameter | Tested range | Optimum value |
|---------------------------|--------------|---------------|
| Maximum features per tree | 5–24 | 7 |
| Maximum tree depth | 5–100 | 12 |
| Minimum samples split | 2–50 | 5 |
| Minimum samples leaf | 2–50 | 5 |
| Bootstrap | True, False | True |

lowed us to come up with a revised structural interpretation of CA (Fig. 9), further highlighting the value of our approach. Exploration geologists at CA have since validated aspects of this spectral interpretation through targeted field mapping of the purple shale unit and folded CA conglomerate.

The RF results also highlight some challenges that could be addressed in future studies. Firstly, a comparison of the classification results with the geology map of Díez-Montes and García-Crespo (2013) suggests that the random forest classifier is not able to accurately distinguish between black shales and massive sulphides. This is unsurprising, as both units are characterised by flat and generally low-reflectance spectra in the VNIR and SWIR. However it is possible that these units could be successfully distinguished using features that highlight subtle differences in the visible and VNIR parts of the spectrum (cf. Fig. 4) or by capturing and integrating long-wave infrared imagery that can better discriminate silicate minerals associated with the mineralization (e.g. quartz).

Secondly, we also interpret that the Sericite A unit associated with oxidised and weathered material along the northern rim of the pit results from supergene clay minerals forming in weathered chlorite volcanics. Unfortunately hand-samples from these locations could not be

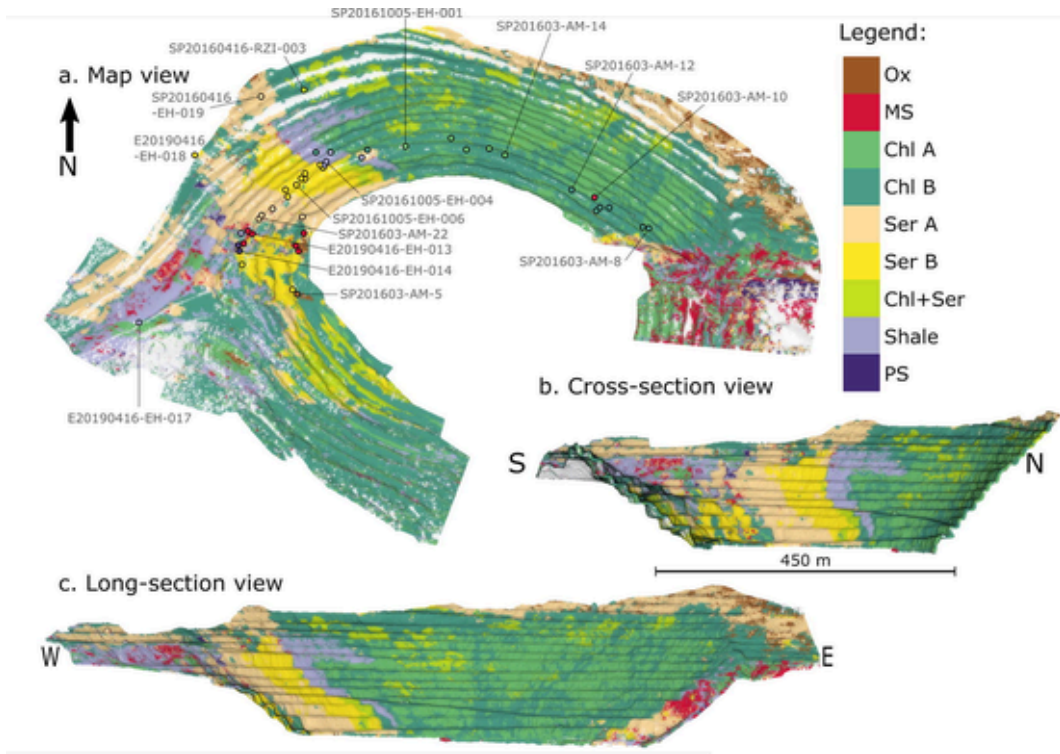


Fig. 8. Map (a), cross-section (b) and long-section (c) views of the RF classification. The hand-samples used to train the RF are overlain in (a) using approximate locations (measured with a handheld GPS) and coloured by their label (cf. Table 1). Samples selected for XRD analyses (Appendix 8) are also highlighted. 3-D visualisations of this classification can be found at <https://tinyurl.com/ca-hypercloud>.

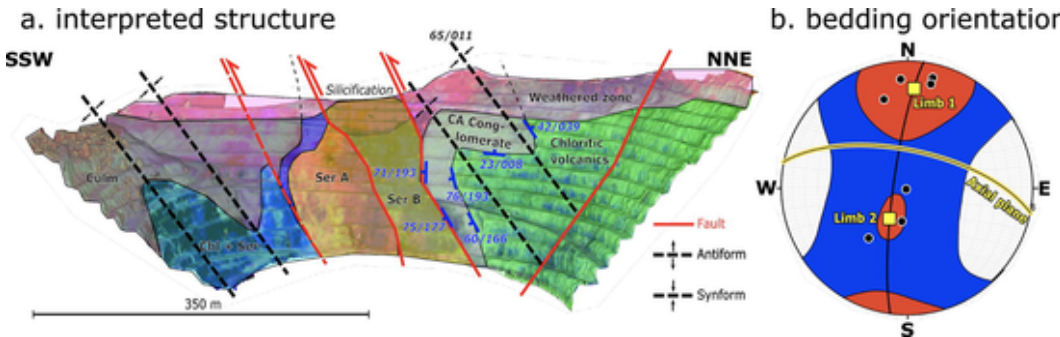


Fig. 9. Schematic structural cross section of the Corta Atalaya open pit based on an interpretation of the hyperspectral mapping results and structural measurements extracted from the 3-D hypercloud. Units are labelled according to Figs. 1 and 8, and draped on the MNF visualisation presented in Fig. 5. Bedding measurements extracted based on these mapping results and the 3-D topography are overlain on (a) and plotted on a lower hemisphere equal-area stereographic projection (b) using Stereonet 11 (Allmendinger, 2020). Contours in (b) were calculated using the Kamb method (Allmendinger et al., 2011) and used to define the average orientation of each fold limb, and hence estimate the orientation of the fold's axial plane.

retrieved (due to access limitations), and so were not included in our training dataset. It is likely that if samples could be retrieved then this supergene zone could be mapped as a distinct lithology by the RF. Similarly, chloritic shales outcropping along the southern margin of the pit could not be distinguished from chloritised volcanics in the north due to a lack of samples from this unit in the training dataset (cf. Fig. 8).

Despite these limitations, our results are a clear demonstration that, with adequate corrections and careful feature selection, hyperspectral information can be quantitatively compared between laboratory and outcrop scales. Even though the random forest classifier was trained exclusively on laboratory-acquired spectral imagery of individual hand samples, it was able to successfully classify the CA hypercloud and extract meaningful geological information. This approach has significant practical advantages over traditional methods because the need for subjective, labour-intensive and potentially unsafe field-mapping to create training labels is reduced.

This approach is made possible by the intimate integration of geometric and spectral data via a hypercloud. Previous state-of-the-art approaches (e.g., Krupnik and Khan, 2019) are limited by confounding atmospheric and illumination effects, which reduce the accuracy of automatic mapping methods. The integration of high-resolution geometry into the spectral processing workflow allows significantly better correction of these effects, and thus more accurate spectral derivatives and classifications. Previous methods for co-registering 3-D geometry with spectral data (e.g., Jakob et al., 2017) have been limited by inaccurate and laborious methods for estimating the position and orientation of the hyperspectral sensor. The PnP solution implemented in *hylite* circumvents these issues and allows many different hyperspectral datasets to be back-projected and fused into a hypercloud. The value of these data is further enhanced by the associated high-resolution geometry, as this 3-D information is critical for interpreting the geometry of geological bodies. This is exemplified by our ability to map folded units at CA, visualise the results in 3-D, and extract structural measurements that constrain the fold's axial plane (Fig. 9).

Finally, our results also suggest that some hyperspectral derivatives (e.g. minimum wavelength maps and band ratios) are relatively scale-invariant for properly corrected datasets. This raises the interesting possibility that ML algorithms trained on libraries of hand-samples could aid mapping activities at larger scales and become “digital geologists” that assist interpretation efforts by objectively converting HSI data from drill core, outcrop, mine-face and airborne campaigns into lithological maps and logs. This would provide a unified approach that ameliorates issues with inconsistent logging and mapping which commonly plague minerals exploration, and in doing so facilitate efforts to synthesise and homogenize regional datasets. It also provides a mechanism for generating the large and robust training datasets that are critical for the successful application of modern machine learning methods.

7. Conclusion

The open-source *hylite* package provides a uniform workflow for fusing raw hyperspectral data from multiple sensors and acquisition geometries into radiometrically and geometrically corrected 3-D hyperclouds. The package can then be used to derive geologically relevant data products, such as minimum wavelength maps, band ratios and spectral classifications. To demonstrate this, we used *hylite* to combine 10 ground-based and 357 UAV-borne hyperspectral images into a single reflectance hypercloud. This was used to map lithology and alteration mineralogy to at the Corta Atalaya mine and (1) characterise the structure and geometry of the rocks hosting the deposit, and (2) identify subtle changes in alteration mineralogy that could be used as mineralization vectors. These results highlight the potential of hyperspectral imaging for rapid and objective mine-face mapping and core-logging, both of which are essential to modern mining, exploration and ore-deposit research.

Declaration of Competing Interest

The authors declare that they have no known competing financial interests or personal relationships that could have appeared to influence the work reported in this paper.

Acknowledgements

The authors would like to acknowledge extensive support from Atalaya Mining during fieldwork conducted for this publication, and subsequent validation of the results. This research also received funding from the European Union's Horizon 2020 research and innovation program under grant agreement No 776487. ST was supported with funding from Total. Robert Zimmermann is gratefully acknowledged for field assistance. Doreen Ebert, Juan-Felipe Bustos and Naomi Brazzo are acknowledged for helping with sample preparation and drafting figures. We would also like to thank Laurent Ailleres and an anonymous reviewer for their insightful and constructive comments.

Appendix A. Supplementary data

Supplementary data to this article can be found online at <https://doi.org/10.1016/j.oregeorev.2021.104252>.

References

- Aasen, H., Honkavara, E., Lucier, A., Zarco-Tejada, P.J., 2018. Quantitative remote sensing at ultra-high resolution with UAV spectroscopy: A review of sensor technology, measurement procedures, and data correction workflows. *Remote Sens.* 10, 1091. <https://doi.org/10.3390/rs10071091>.
- Acosta, I.C.C., Khodadadzadeh, M., Tusa, L., Ghamisi, P., Gloaguen, R., 2019. A machine learning framework for drill-core mineral mapping using hyperspectral and high-resolution mineralogical data fusion. *IEEE J. Sel. Top. Appl. Earth Obs. Remote Sens.* 12, 4829–4842. <https://doi.org/10.1109/JSTARS.2019.2924292>.
- Allmendinger, R.W., 2020. Stereonet 11.
- Allmendinger, R.W., Cardozo, N., Fisher, D.M., 2011. Structural geology algorithms: Vectors and tensors. Cambridge University Press.
- Bemis, S.P., Micklethwaite, S., Turner, D., James, M.R., Akciz, S., Thiele, S.T., Bangash, H.A., 2014. Ground-based and UAV-Based photogrammetry: A multi-scale, high-resolution mapping tool for structural geology and paleoseismology. *J. Struct. Geol.* 69, 163–178. <https://doi.org/10.1016/j.jsg.2014.10.007>.
- Boggs, T., 2014. Spectral Python (SPY).
- Boubanga-Tombet, S., Huot, A., Vitins, I., Heuberger, S., Veuve, C., Eisele, A., Hewson, R., Guyot, E., Marcotte, F., Chamberland, M., 2018. Thermal infrared hyperspectral imaging for mineralogy mapping of a mine face. *Remote Sens.* 10, 1518.
- Bradski, G., Kaehler, A., 2008. Learning OpenCV: Computer vision with the OpenCV library. O'Reilly Media, Inc.
- Breiman, L., 2001. Random forests. *Mach. Learn.* 45, 5–32.
- Buckley, S.J., Kurz, T.H., Howell, J.A., Schneider, D., 2013. Terrestrial lidar and hyperspectral data fusion products for geological outcrop analysis. *Comput. Geosci.* 54, 249–258. <https://doi.org/10.1016/j.cageo.2013.01.018>.
- Clark, R.N., Swayze, G.A., Livo, K.E., Kokaly, R.F., Sutley, S.J., Dalton, J.B., McDougal, R.R., Gent, C.A., 2003. Imaging spectroscopy: Earth and planetary remote sensing with the USGS Tetracorder and expert systems. *J. Geophys. Res. Planets* 108 (E12).
- Cudahy, T., Jones, M., Thomas, M., Laukamp, C., Caccetta, M., Hewson, R., Rodger, A., Verrall, M., 2008. Next generation mineral mapping: Queensland airborne HyMap and satellite ASTER surveys 2006–2008. Perth Publicly Available Rep. P2007364 152.
- Dering, G.M., Micklethwaite, S., Thiele, S.T., Vollgger, S.A., Cruden, A.R., 2019. Review of drones, photogrammetry and emerging sensor technology for the study of dykes: Best practices and future potential. *J. Volcanol. Geotherm. Res.* 373, 148–166. <https://doi.org/10.1016/j.jvolgeores.2019.01.018>.
- Díez-Montes, A., Bellido Mulas, F., Sánchez-García, T., García-Crespo, J., 2017. Lithogeochemistry of Volcanic Rocks in the Río Tinto Mine, Iberian Pyrite Belt (Huelva, Spain). Instituto Geológico y Minero de España, Madrid.
- Díez-Montes, A., García-Crespo, J., 2013. Geological map of the Río Tinto area, 1: 10,000.
- Fraser, S., Whitbourn, L.B., Yang, K., Ramanaidou, E., Connor, P., Poropat, G., Soole, P., Mason, P., Coward, D., Phillips, R., 2006. Mineralogical face-mapping using hyperspectral scanning for mine mapping and control. In: Australasian Institute of Mining and Metallurgy Publication Series. Presented at the 6th International Mining Geology Conference. pp. 21–23.
- Girardeau-Montaut, D., 2020. CloudCompare.
- Green, A.A., Berman, M., Switzer, P., Craig, M.D., 1988. A transformation for

- ordering multispectral data in terms of image quality with implications for noise removal. *IEEE Trans. Geosci. Remote Sens.* 26, 65–74. <https://doi.org/10.1109/36.3001>.
- Haest, M., Cudahy, T., Laukamp, C., Gregory, S., 2012. Quantitative mineralogy from infrared spectroscopic data. I. Validation of mineral abundance and composition scripts at the Rocklea channel iron deposit in Western Australia. *Econ. Geol.* 107 (2), 209–228.
- Harris, C.R., Millman, K.J., van der Walt, S.J., Gommers, R., Virtanen, P., Cournapeau, D., Wieser, E., Taylor, J., Berg, S., Smith, N.J., Kern, R., Picus, M., Hoyer, S., van Kerkwijk, M.H., Brett, M., Haldane, A., del Río, J.F., Wiebe, M., Peterson, P., Gérard-Marchant, P., Sheppard, K., Reddy, T., Weckesser, W., Abbasi, H., Gohlke, C., Oliphant, T.E., 2020. Array programming with NumPy. *Nature* 585, 357–362. <https://doi.org/10.1038/s41586-020-2649-2>.
- Hecker, C., van Ruitenbeek, F.J.A., van der Werff, H.M.A., Bakker, W.H., Hewson, R.D., van der Meer, F.D., 2019. Spectral absorption feature analysis for finding ore: A tutorial on using the method in geological remote sensing. *IEEE Geosci. Remote Sens. Mag.* 7, 51–71. <https://doi.org/10.1109/MGRS.2019.2899193>.
- Honkavaara, E., Eskelinen, M.A., Pölonen, I., Saari, H., Ojanen, H., Mannila, R., Holmlund, C., Hakala, T., Litkey, P., Rosnell, T., 2016. Remote sensing of 3-D geometry and surface moisture of a peat production area using hyperspectral frame cameras in visible to short-wave infrared spectral ranges onboard a small unmanned airborne vehicle (UAV). *IEEE Trans. Geosci. Remote Sens.* 54, 5440–5454.
- Honkavaara, E., Kaivosoja, J., Mäkinen, J., Pellikka, I., Pesonen, L., Saari, H., Salo, H., Hakala, T., Markelin, L., Rosnell, T., 2012. Hyperspectral reflectance signatures and point clouds for precision agriculture by light weight UAV imaging system. *ISPRS Ann. Photogram. Remote Sens. Spat. Inf. Sci.* 7, 353–358.
- Inverno, C., Díez-Montes, A., Rosa, C., García-Crespo, J., Matos, J., García-Lobón, J.L., Carvalho, J., Bellido, F., Castello-Branco, J.M., Ayala, C., Batista, M.J., Rubio, F., Granado, I., Tornos, F., Oliveira, J.T., Rey, C., Araújo, V., Sánchez-García, T., Pereira, Z., Represas, P., Solá, A.R., Sousa, P., 2015. Introduction and Geological Setting of the Iberian Pyrite Belt, in: Weihed, P. (Ed.), 3D, 4D and Predictive Modelling of Major Mineral Belts in Europe, Mineral Resource Reviews. Springer International Publishing, Cham, pp. 191–208. https://doi.org/10.1007/978-3-319-17428-0_9.
- Jakob, S., Zimmermann, R., Gloaguen, R., 2017. The need for accurate geometric and radiometric corrections of drone-borne hyperspectral data for mineral exploration: MEPHYSTO—A Toolbox for pre-processing drone-borne hyperspectral data. *Remote Sens.* 9, 88. <https://doi.org/10.3390/rs9010088>.
- Kirsch, M., Lorenz, S., Zimmermann, R., Andreani, L., Tusa, L., Pospiech, S., Jackisch, R., Khodadadzadeh, M., Ghamisi, P., Unger, G., Hödl, P., Gloaguen, R., Middleton, M., Sutinen, R., Ojala, A., Mattila, J., Nordbäck, N., Palmu, J.-P., Tiljander, M., Ruskeniemi, T., 2019. Hyperspectral outcrop models for palaeoseismic studies. *Photogram. Rec.* 34, 385–407. <https://doi.org/10.1111/phor.12300>.
- Kirsch, M., Lorenz, S., Zimmermann, R., Tusa, L., Möckel, R., Hödl, P., Booyens, R., Khodadadzadeh, M., Gloaguen, R., 2018. Integration of terrestrial and drone-borne hyperspectral and photogrammetric sensing methods for exploration mapping and mining monitoring. *Remote Sens.* 10, 1366. <https://doi.org/10.3390/rs10091366>.
- Kluyver, T., Ragan-Kelley, B., Pérez, F., Granger, B.E., Bussanier, M., Frederic, J., Kelley, K., Hamrick, J.B., Grout, J., Corlay, S., 2016. Jupyter Notebooks—a publishing format for reproducible computational workflows, in: *ELPUB*, pp. 87–90.
- Krupnik, D., Khan, S., 2019. Close-range, ground-based hyperspectral imaging for mining applications at various scales: Review and case studies. *Earth Sci. Rev.* 198, 102952.
- Kruse, F.A., Bedell, R.L., Taranik, J.V., Peppin, W.A., Weatherbee, O., Calvin, W.M., 2012. Mapping alteration minerals at prospect, outcrop and drill core scales using imaging spectrometry. *Int. J. Rem. Sens.* 33 (6), 1780–1798.
- Kurz, T.H., Buckley, S.J., Howell, J.A., Schneider, D., 2011. Integration of panoramic hyperspectral imaging with terrestrial lidar data. *Photogram. Rec.* 26, 212–228. <https://doi.org/10.1111/j.1477-9730.2011.00632.x>.
- Laukamp, C., Rodger, A., LeGras, M., Lampinen, H., Lau, I.C., Pejic, B., Stromberg, J., Francis, N., Ramanaidou, E., 2021. Mineral physicochemistry underlying feature-based extraction of mineral abundance and composition from shortwave, mid and thermal infrared reflectance spectra. *Minerals* 11 (4), 347.
- Leistel, J.M., Marcoux, E., Thiéblemont, D., Quesada, C., Sánchez, A., Almodóvar, G.R., Pascual, E., Sáez, R., 1997. The volcanic-hosted massive sulphide deposits of the Iberian Pyrite Belt Review and preface to the Thematic Issue. *Miner. Deposita* 33, 2–30.
- Loh, E., 1973. Optical vibrations in sheet silicates. *J. Phys. C Solid State Phys.* 6 (6), 1091.
- Lorenz, S., Salehi, S., Kirsch, M., Zimmermann, R., Unger, G., Vest Sørensen, E., Gloaguen, R., 2018. Radiometric correction and 3D integration of long-range ground-based hyperspectral imagery for mineral exploration of vertical outcrops. *Remote Sens.* 10, 176. <https://doi.org/10.3390/rs10020176>.
- Lowe, D.G. 1999. Object recognition from local scale-invariant features, in: *Proceedings of the Seventh IEEE International Conference on Computer Vision*, Presented at the Proceedings of the Seventh IEEE International Conference on Computer Vision, pp. 1150–1157 vol. 2. <https://doi.org/10.1109/ICCV.1999.790410>.
- Martin-Izard, A., Arias, D., Arias, M., Gumiel, P., Sanderson, D.J., Castañón, C., Lavandeira, A., Sanchez, J., 2015. A new 3D geological model and interpretation of structural evolution of the world-class Rio Tinto VMS deposit, Iberian Pyrite Belt (Spain). *Ore Geol. Rev.* 71, 457–476. <https://doi.org/10.1016/j.oregeorev.2015.06.006>.
- Muja, M., Lowe, D.G., 2009. Fast approximate nearest neighbors with automatic algorithm configuration. *VISAPP 1* (2), 2.
- Murphy, R.J., Monteiro, S.T., 2013. Mapping the distribution of ferric iron minerals on a vertical mine face using derivative analysis of hyperspectral imagery (430–970 nm). *ISPRS J. Photogramm. Remote Sens.* 75, 29–39.
- Murphy, R.J., Taylor, Z., Schneider, S., Nieto, J., 2015. Mapping clay minerals in an open-pit mine using hyperspectral and LiDAR data. *Eur. J. Remote Sens.* 48, 511–526.
- Nesbit, P.R., Durkin, P.R., Hugenholtz, C.H., Hubbard, S.M., Kucharczyk, M., 2018. 3-D stratigraphic mapping using a digital outcrop model derived from UAV images and structure-from-motion photogrammetry. *Geosphere* 14, 2469–2486. <https://doi.org/10.1130/GES01688.1>.
- Pedregosa, F., Varoquaux, G., Gramfort, A., Michel, V., Thirion, B., Grisel, O., Blondel, M., Prettenhofer, P., Weiss, R., Dubourg, V., 2011. Scikit-learn: Machine learning in Python. *J. Mach. Learn. Res.* 12, 2825–2830.
- Pontual, S., Merry, N., Gamsou, P., 1997. G-Mex Spectral Interpretation Field Manual. AusSpec international, Sydney.
- Quesada, C., 1997. A reappraisal of the structure of the Spanish segment of the Iberian Pyrite Belt. *Miner. Deposita* 33, 31–44. <https://doi.org/10.1007/s001260050131>.
- Ramanaidou, E.R., Wells, M.A. 2012. Hyperspectral imaging of iron ores, in: *Proceedings of the 10th International Congress for Applied Mineralogy (ICAM)*. Springer, pp. 575–580.
- Rother, C., Kolmogorov, V., Blake, A., 2004. “GrabCut”: Interactive Foreground Extraction Using Iterated Graph Cuts, in: *ACM SIGGRAPH 2004 Papers on - SIGGRAPH '04*. ACM Press, Los Angeles, California, p. 309. <https://doi.org/10.1145/1186562.1015720>.
- Salehi, S., Lorenz, S., Vest Sørensen, E., Zimmermann, R., Fensholt, R., Henning Heincke, B., Kirsch, M., Gloaguen, R., 2018. Integration of vessel-based hyperspectral scanning and 3D-photogrammetry for mobile mapping of steep coastal cliffs in the Arctic. *Remote Sens.* 10, 175. <https://doi.org/10.3390/rs10020175>.
- Sonntag, I., Laukamp, C., Hagemann, S.G., 2012. Low potassium hydrothermal alteration in low sulfidation epithermal systems as detected by IRS and XRD: An example from the Co-O mine, Eastern Mindanao, Philippines. *Ore Geol. Rev.* 45, 47–60.
- Soriano, C., Martí, J., 1999. Facies analysis of volcano-sedimentary successions hosting massive sulfide deposits in the Iberian pyrite belt, Spain. *Econ. Geol.* 94, 867–882. <https://doi.org/10.2113/gsecongeo.94.6.867>.
- Thiele, S.T., Grose, L., Samsu, A., Micklethwaite, S., Vollgger, S.A., Cruden, A.R., 2017. Rapid, semi-automatic fracture and contact mapping for point clouds, images and geophysical data. *Solid Earth* 8, 1241.
- Tusa, L., Kern, M., Khodadadzadeh, M., Blannin, R., Gloaguen, R., Gutzmer, J., 2020. Evaluating the performance of hyperspectral short-wave infrared sensors for the pre-sorting of complex ores using machine learning methods. *Miner. Eng.* 146, 106150. <https://doi.org/10.1016/j.mineng.2019.106150>.
- van der Meer, F., Kopačková, V., Koucká, L., van der Werff, H.M.A., van Ruitenbeek, F.J.A., Bakker, W.H., 2018. Wavelength feature mapping as a proxy to mineral chemistry for investigating geologic systems: An example from the Rodalquilar epithermal system. *Int. J. Appl. Earth Obs. Geoinformation* 64, 237–248. <https://doi.org/10.1016/j.jag.2017.09.008>.
- van der Meer, F.D., van der Werff, H.M.A., van Ruitenbeek, F.J.A., Hecker, C.A., Bakker, W.H., Noomen, M.F., van der Meijde, M., Carranza, E.J.M., de Smeth, J.B., Woldai, T., 2012. Multi- and hyperspectral geologic remote sensing: A review. *Int. J. Appl. Earth Obs. Geoinformation* 14, 112–128. <https://doi.org/10.1016/j.jag.2011.08.002>.
- van Ruitenbeek, F.J., Bakker, W.H., van der Werff, H.M., Zegers, T.E., Oosthoek, J.H., Omer, Z.A., Marsh, S.H., van der Meer, F.D., 2014. Mapping the wavelength position of deepest absorption features to explore mineral diversity in hyperspectral images. *Planet. Space Sci.* 101, 108–117.
- Vedder, W., McDonald, R.S., 1963. Vibrations of the OH ions in muscovite. *J. Chem. Phys.* 38 (7), 1583–1590.
- Weinzaepfel, P., Revaud, J., Harchaoui, Z., Schmid, C., 2013. DeepFlow: Large displacement optical flow with deep matching. In: *Proceedings of the IEEE International Conference on Computer Vision*, pp. 1385–1392.
- Yang, K., Whitbourn, L., Mason, P., Huntington, J., 2013. Mapping the chemical composition of nickel laterites with reflectance spectroscopy at Koniambo, New Caledonia. *Econ. Geol.* 108, 1285–1299.
- Zhong, Y., Wang, X., Xu, Y., Wang, S., Jia, T., Hu, X., Zhao, J., Wei, L., Zhang, L., 2018. Mini-UAV-borne hyperspectral remote sensing: From observation and processing to applications. *IEEE Geosci. Remote Sens. Mag.* 6, 46–62. <https://doi.org/10.1109/MGRS.2018.2867592>.